

## Full Rotational Dynamics of Plastic Microfibers in Turbulence

Vlad Giurgiu<sup>1</sup>, Giuseppe Carlo Alp Caridi<sup>1</sup>, Marco De Paoli<sup>1,2</sup> and Alfredo Soldati<sup>1,3,\*</sup>

<sup>1</sup>*Institute of Fluid Mechanics and Heat Transfer, TU Wien, 1060 Wien, Austria*

<sup>2</sup>*Physics of Fluids Group, University of Twente, 7500AE Enschede, Netherlands*

<sup>3</sup>*DPIA, University of Udine, 33100 Udine, Italy*



(Received 14 February 2024; accepted 17 June 2024; published 2 August 2024)

The motion, settling, and dispersion of microplastics in the ocean are determined by their rotational dynamics. We present experiments on elongated, large aspect ratio, and mildly curved plastic fibers slightly longer than the Kolmogorov length scale. Exploiting their uniquely identifiable three-dimensional orientation, we perform original optical Lagrangian investigations and provide a set of homogeneous data on their rotation rates around their longitudinal axis: spinning rate, and transversal axes: tumbling rates, which we explain in the context of the general features of turbulence.

DOI: 10.1103/PhysRevLett.133.054101

Turbulent flows with suspended anisotropic particles are ubiquitous [1,2] in many industrial [3,4] and natural processes [5–7]. The motion, dispersion, and sedimentation rate of anisotropic particles depend on their rotational dynamics. The recent and sudden increase of attention on the dynamics of such particles is driven by the growing concern about ocean microplastics pollution [8–14]. Most oceanic microplastics are small and elongated microfibers [15,16] and their dynamics depend on the forces and torques applied by the smallest turbulence scales [17,18]. However, even if the statistical properties of turbulence at the smallest scale are rather well established and given that no closed form of the drag on nonspherical particles is available, a predictive understanding of the dynamics of anisotropic particles remains elusive. The full rotational dynamics of a small elongated particle is given by the rotation rates around the three principal axes: spinning rate—around the longitudinal axis, and tumbling rates—around the two transversal axes. Current numerical [19–23] and experimental investigations [17,24–26] are limited to tumbling rates of small slender objects. The present study takes advantage of the specific shape of the investigated particles, which are microplastic slender fibers with aspect ratio  $\sim 100$  and a slight curvature: these fibers behave like elongated ellipsoids [1], but their slight curvature provides the complete information on their three-dimensional orientation, and allows measurements of rotation rates around their three axes. We focus on wall-bounded turbulence, confirm previous measurements of fiber tumbling obtained in different flow configurations, boundary layers, and homogeneous isotropic

turbulence (HIT), and discuss the results of each rotational component—spinning and two tumbling rates.

Experiments are performed in the TU Wien Turbulent Water Channel [27], at a shear Reynolds number  $Re_\tau = u_\tau h / \nu = 720$ , where  $u_\tau = 20.5 \text{ mm s}^{-1}$ ,  $\nu = 1.13 \text{ mm}^2 \text{ s}^{-1}$ , and  $h = 40 \text{ mm}$  are the friction velocity, kinematic viscosity, and half-channel height, respectively. Additional methodological details are provided in [28]. In the fully developed turbulent channel flow, the viscous length and timescales are  $\delta_\nu = \nu / u_\tau = 55 \text{ }\mu\text{m}$  and  $\tau = \delta_\nu / u_\tau = 2.7 \text{ ms}$ , [27]. The Kolmogorov length [ $\eta = (\nu^3 / \epsilon)^{1/4}$ ] and timescales [ $\tau_\eta = (\nu / \epsilon)^{1/2}$ ] vary between wall and channel center in the range  $\eta = 83\text{--}286 \text{ }\mu\text{m}$  and  $\tau_\eta = 5.7\text{--}75 \text{ ms}$ , respectively, where  $\epsilon$  is the turbulent kinetic energy dissipation rate. To obtain the values for the Kolmogorov time and length scales we interpolated values of previous direct numerical simulations (DNS) at  $Re_\tau = 590$  [35] and  $Re_\tau = 950$  [36]. Fibers have a density of  $\rho_f = 1.15 \text{ g cm}^{-3}$  (see [28] and [37] for details about their settling behavior), are  $l = 1.2 \text{ mm}$  long and  $d = 10 \text{ }\mu\text{m}$  in diameter (aspect ratio  $\lambda = l/d = 120$ ) [38]. Relative to the local Kolmogorov length scale,  $l$  ranges between  $4.2\eta$  and  $11.4\eta$ , from the channel center to  $2 \text{ mm}$  above the wall, respectively. At  $Re_\tau = 720$ , they are rigid and inertia-less with a translational Stokes number [39]  $St \sim \mathcal{O}(10^{-2})$  [40]. The tumbling Stokes number [41] is  $St_t \sim \mathcal{O}(10^{-5})$ . Fibers are dispersed in water to form a dilute suspension with a volume fraction of  $\mathcal{O}(10^{-9})$ , with negligible interparticle interactions and influence on the flow [2]. Measurements are performed at two wall-normal locations,  $y^+ = y/\delta_\nu < 270$  and  $640 < y^+ < 800$ . The laser-illuminated fibers are imaged with six high-speed cameras [27] to reconstruct their shape and measure their dynamics [42]. In Fig. 1, we show as dark gray voxels the tomographic reconstruction of the light scattered by one

\*Contact author: alfredo.soldati@tuwien.ac.at

Also at: Polytechnic Department, University of Udine, 33100 Udine, Italy.

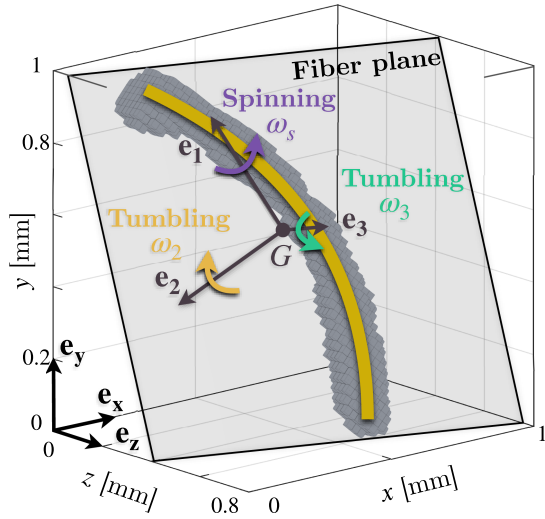


FIG. 1. A reconstructed fiber (dark gray voxels), its fitted polynomial (yellow line), the fiber-fixed axes ( $\mathbf{e}_1, \mathbf{e}_2, \mathbf{e}_3$ ), and its center of mass  $G$  (black dot) are shown. Spinning ( $\omega_s$ ) and tumbling rate components ( $\omega_2, \omega_3$ ) around these axes are noted [1]. The laboratory reference frame is indicated by  $\mathbf{e}_x$  (streamwise),  $\mathbf{e}_y$  (wall-normal), and  $\mathbf{e}_z$  (spanwise).

fiber (see [28]). Fibers are contained in a plane (light gray plane) [40,42], with their center of mass ( $G$ ) and eigenvectors of their inertia tensor ( $\mathbf{e}_1, \mathbf{e}_2, \mathbf{e}_3$ —in order of ascending eigenvalues) defining their position and orientation. A 2nd order polynomial (yellow line in Fig. 1) is fitted to the reconstructed fiber to measure its curvature. All statistics have been computed with fibers having a curvature in a limited range. Consult [28] for the distribution of the fibers' curvature and the considered range. In the fiber reference frame, the spinning rate,  $\omega_s$  is defined as the rotation rate around  $\mathbf{e}_1$  and the two tumbling rate components,  $\omega_2$  and  $\omega_3$  as the rotation rates around  $\mathbf{e}_2$  and  $\mathbf{e}_3$ , respectively [1]. In the laboratory reference frame, rotation

rates around  $\mathbf{e}_x$  (streamwise),  $\mathbf{e}_y$  (wall-normal), and  $\mathbf{e}_z$  (spanwise) directions are  $\omega_x, \omega_y$ , and  $\omega_z$ , respectively (see [28]).

The richness of the present measurements is demonstrated by a fiber trajectory near the wall in Fig. 2. This fiber moves  $\mathcal{O}(500\delta_\nu)$  in the streamwise ( $x^+$ ) and  $\mathcal{O}(30\delta_\nu)$  in the wall-normal ( $y^+$ ) and spanwise ( $z^+$ ) directions. Its trajectory is colored by its spinning rate scaled by the track average (denoted with  $\bar{\cdot}$ ). The fiber is shown magnified at three different times to illustrate the temporal change of its orientation, defined by the three vectors  $\mathbf{e}_1, \mathbf{e}_2$ , and  $\mathbf{e}_3$ . The traces of the fiber's center of mass onto the Cartesian planes are also shown, with those onto planes  $xz$  and  $xy$  being colored by  $\omega_2$  and  $\omega_3$ , respectively, and scaled by their track average.

The length scales and timescales of turbulence increase from the wall towards the channel center, where turbulence features are similar to HIT. We focus first on the channel center region. In Fig. 3 we show the probability density function (PDF) of the squared tumbling rate  $\omega_t^2 = \omega_2^2 + \omega_3^2$  normalized by its average value,  $\langle \omega_t^2 \rangle$ , computed over the entire dataset and indicated here by angular brackets. The comparison with measurements ( $l/\eta = 4.9$ ) [43] and direct numerical simulations (DNS) of rods ( $l/\eta = 1$ ) [17] shows excellent agreement, particularly in the distribution's long tails, where rare, strong rotation rate events occur. DNS data exhibit slightly larger rotation rates at high values of normalized squared tumbling rates. This is possibly due to the effect of the fiber's finite length in the experiments and the assumption of tracing, pointwise fibers in DNS. Consult [28] for the effect of sample size on the PDF of tumbling rates. The slight curvature of fibers appears to have no discernible effect on the PDF of tumbling rates. Consult [28] for the effect of curvature on rotation rates.

Previous observations have shown that the tumbling rate is a strong function of the wall distance, with fibers tumbling faster near the wall [21,24,25,40,44,45]. In the

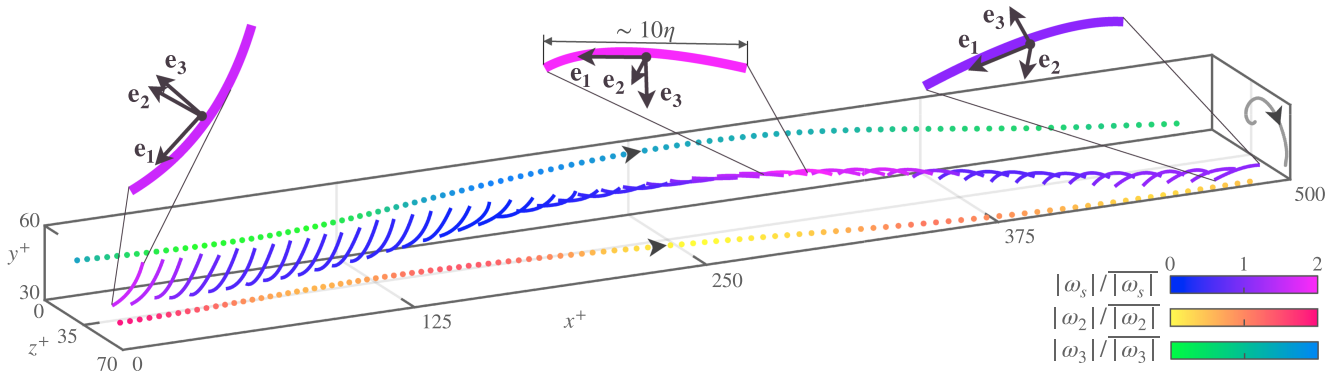


FIG. 2. A 3D view of a fiber trajectory, showing its center of mass on  $xz$ ,  $xy$  (color indicates  $|\omega_2|, |\omega_3|$ ), and  $yz$  planes (gray line). The black arrows indicate its progression. The fiber-equivalent polynomial is colored by  $|\omega_s|$ . The rotation rates are normalized with their corresponding mean absolute track value of  $|\overline{\omega_s}| = 1908$ ,  $|\overline{\omega_2}| = 731$ , and  $|\overline{\omega_3}| = 665^\circ\text{s}^{-1}$ . Above, three instances in time are magnified. The black vectors ( $\mathbf{e}_1, \mathbf{e}_2$ , and  $\mathbf{e}_3$ ) are the reference frame fixed to the fiber (see Fig. 1). The fiber's end-to-end length relative to the Kolmogorov scale ( $\eta$ ) near the wall is noted.

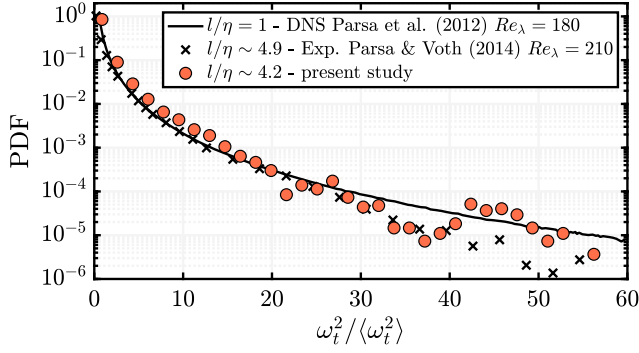


FIG. 3. PDF of the normalized tumbling rate measured in the center of the channel (red circle) compared to numerical simulations of straight rods with  $l/\eta = 1$  ([17], black line) and experiments  $l/\eta \sim 4.9$  ([43],  $\times$ ) in HIT.  $Re_\lambda$  is the Taylor Reynolds number.

main panel of Fig. 4, the mean squared tumbling rate normalized by the viscous timescale as a function of the  $\delta_\nu$ -scaled wall distance is shown (see [28]). The present data are compared with measurements in a boundary layer at  $Re_\tau = 620$ , with fibers 2.4 times longer than the present ones [24]. As a reference, we show measurements in HIT of fibers 1 order of magnitude longer than  $\eta$  [43,46] and with maximum aspect ratio of  $\approx 10$ . Present values of tumbling rates exhibit the same qualitative behavior of previous data [24], with values higher in the wall region and decreasing towards the center of the channel. The high tumbling rates compared to Ref. [24] may be due to the shorter length of our fibers ( $l/\eta \lesssim 11$ —approximately in the dissipative range of turbulence [43]) compared to rods in Ref. [24] ( $22 \lesssim l/\eta \lesssim 42$ —in the inertial subrange, where tumbling rates scale with  $(l/\eta)^{-4/3}$  [43,46]). The different tumbling rates compared to Ref. [24] may not be explained by differences in the translational Stokes number. At  $y^+ = 50$ , Ref. [21] found negligible differences in the root-mean-square of rotation rates between tracer particles ( $St = 0$ ) and rigid fibers ( $\lambda = 50$ ,  $l/\eta \approx 10$ ) at two different Stokes numbers ( $St = 1$  and 5). Furthermore, Ref. [20] reported a reduction of only  $\approx 20\%$  in the mean squared tumbling rate between tracer particles ( $St = 0$ ) and inertial straight fibers ( $St = 30$ ,  $\lambda = 50$ ) at the channel center. The mean squared tumbling rate exhibits a peak at  $y^+ \approx 60$ , which has not been observed in previous experiments. At the channel center, values similar to previous HIT experimental data are recovered [43,46]. Previous experiments on fibers in wall-bounded and HIT turbulence are limited to measuring tumbling rates only. Notable exceptions are Ref. [46] (tumbling and spinning rates of cylinders) and Ref. [47] (solid body rotation rates of jacks and crosses). Examples also include numerical studies with prolate and oblate ellipsoids modeled as point particles and carried out by Ref. [19] (all rotation rates) and Ref. [20] (tumbling and spinning rates). Our measured spinning rates at the channel center are found in good agreement (within 20%) with

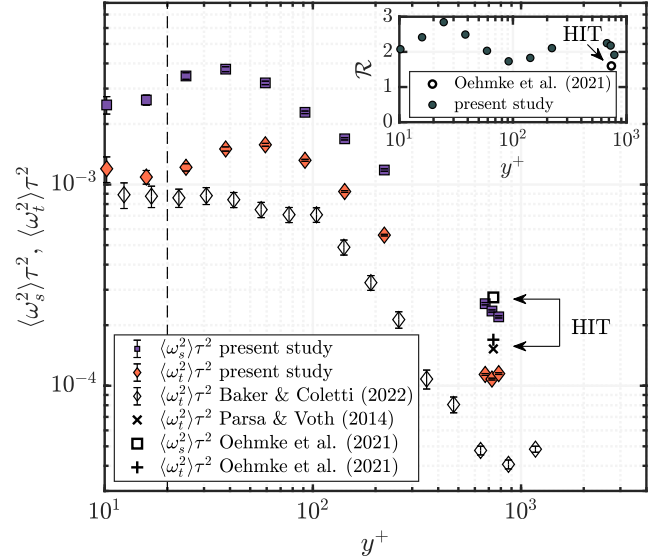


FIG. 4. Main panel: mean square tumbling and spinning rates normalized by the viscous timescale over the wall-normal coordinate. Combined tumbling in the present study ( $l/\eta \approx 4.2$ , red diamond) and straight rods in a turbulent boundary layer ([24],  $l/\eta \approx 22$ – $42$ ,  $Re_\tau = 620$ ,  $St = 6$ , diamond). At the channel center, tumbling measurements of straight rods in HIT  $l/\eta \approx 4.9$  ([43],  $Re_\lambda = 210$ , cross) and  $l/\eta \approx 11$  ([46],  $Re_\lambda = 630$ , +). The fiber length ( $L_f^+ \approx 20$ , —) is displayed. Spinning rate for present experiments ( $l/\eta \approx 4.2$ , purple square) and straight rods in HIT ([46],  $l/\eta \approx 11$ ,  $Re_\lambda = 630$ , square). Error bars represent confidence intervals at 95% and 99% confidence level for data from Ref. [24] and present study, respectively. Note: the values for HIT (cross, plus, and square) are obtained by multiplying the reported values for  $\langle\omega_t^2\rangle\tau_\eta^2$  of 0.12 [43] and 0.13 [46] and for  $\langle\omega_s^2\rangle\tau_\eta^2$  of 0.21 [46] with the ratio  $\tau^2/\tau_\eta^2 = 1.6 \times 10^{-7}$  (here  $\tau_\eta$  is the mean Kolmogorov timescale in the channel central region). Inset: ratio of the mean squared spinning to mean squared tumbling rate  $\mathcal{R} = \langle\omega_s^2\rangle/\langle\omega_t^2\rangle$  for the present study ( $l/\eta \approx 4.2$ , green circle) over the wall-normal coordinate. At the channel center, the measured ratio for HIT ([46],  $l/\eta \approx 11$ ,  $Re_\lambda = 630$ , circle). Arrows indicate measurements in HIT configuration.

those of longer, lower aspect ratio, straight rods in HIT [43,46]. While the spinning rate trends qualitatively similar to tumbling, its peak occurs at  $y^+ \approx 40$ . The inset of Fig. 4 displays the ratio ( $\mathcal{R}$ ) of the mean squared spinning to mean squared tumbling rates as a function of the wall-normal coordinate and is compared with measurements in HIT [46].  $\mathcal{R}$  consistently exceeds unity, reaching up to three (at  $y^+ \approx 25$ ). Near the channel center, the ratio agrees fairly with HIT experiments [46]. This corroborates other studies [19,20,48] that also reported spinning rates higher than tumbling rates. This was attributed by Ref. [46] to rods being preferentially trapped in elongated vortical structures, which have been described by Refs. [49,50] in HIT. In wall-bounded flows, such coherent structures, are typically oriented in the streamwise direction [51–56]. In

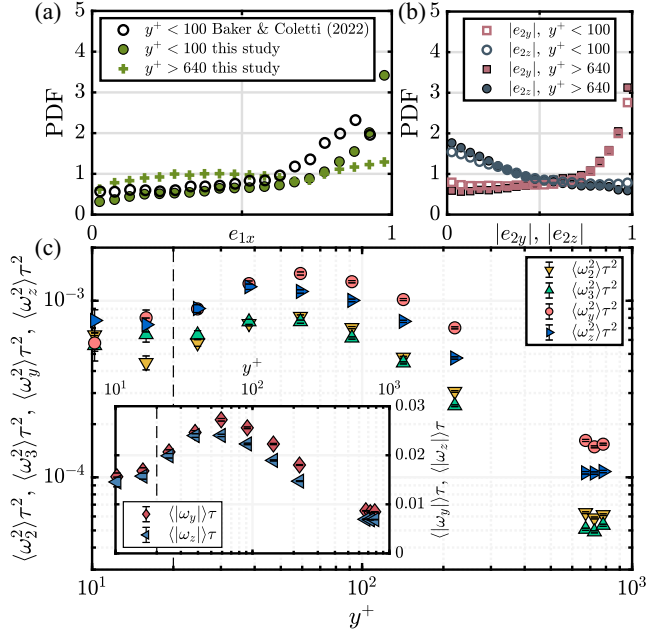


FIG. 5. Panel (a): PDF of the streamwise component of the longitudinal axis vector ( $e_{1x}$ ) in the present study for  $y^+ < 100$  (green circle) and  $640 < y^+ < 800$  ( $+$ ) compared to straight rods in a turbulent boundary layer ([24], circle). Panel (b): PDF of the absolute wall-normal ( $e_{2y}$  for  $y^+ < 100$ , open square and  $640 < y^+ < 800$ , filled square) and spanwise ( $e_{2z}$  for  $y^+ < 100$ , circle and  $640 < y^+ < 800$ , blue circle) components of the transversal axis vector  $\mathbf{e}_2$ . Main panel of (c): mean squared components of tumbling scaled by the viscous time: second (yellow down-pointing triangle) and third (green up-pointing triangle) over  $y^+$ . Mean squared wall-normal (red circle) and spanwise (blue right pointing triangle) rotation rates over  $y^+$ . Inset of panel c): mean absolute wall-normal (Red diamond) and spanwise (blue left pointing triangle) rotation rates over  $y^+$ . Error bars represent confidence intervals at 99% confidence level.

Ref. [20], in agreement with Refs. [23–25,40,44,57,58], a high probability of a streamwise alignment of the longitudinal axis of inertia-less rods ( $St = 0$ ) near the wall (at  $y^+ \approx 10$ ) was observed. Considering the perpendicular alignment of rods to vorticity (mainly oriented in  $\mathbf{e}_z$ ), it was argued by Ref. [20] that the mean shear cannot explain tumbling rates weaker than spinning rates, and this was attributed to the transport and interaction of inertia-less rods with coherent structures, resulting in the preferential streamwise alignment of rods.

Advancing previous studies, in which only the orientation of the longitudinal axis was measured, this study investigates the orientation of all fiber axes:  $\mathbf{e}_1$ ,  $\mathbf{e}_2$ , and  $\mathbf{e}_3$ . In Fig. 5(a) we show the PDF of the streamwise component ( $e_{1x}$ ) of  $\mathbf{e}_1$ , of our fibers and that of straight rods [24]. We consider two flow regions. In the near-wall region (here  $y^+ < 100$ ), the PDF peaks near unity, indicating a preferential alignment of the longitudinal fiber axis with the streamwise direction ( $\mathbf{e}_1 \approx \mathbf{e}_x$ ). While a fair agreement with Ref. [24] is observed, our measured streamwise alignment

is stronger, as evidenced by the narrower distribution. The streamwise orientation near the wall ( $y^+ < 50$ ) has been also observed in numerical studies [59,60]. This preferential orientation is attributed to rods aligning with the strongest Lagrangian stretching direction and was observed in wall-bounded [23,58] and homogeneous isotropic turbulence [61]. At the channel center (here  $640 < y^+ < 800$ ) and consistent with previous studies [20,24,44], the probability of alignment is less than half of that near the wall. In Fig. 5(b) we show the PDF of the absolute wall-normal ( $e_{2y}$ ) and spanwise ( $e_{2z}$ ) components of  $\mathbf{e}_2$  in the same regions as in Fig. 5(a). In both regions, a preferential alignment with the wall-normal direction ( $\mathbf{e}_2 \approx \mathbf{e}_y$ ) is observed, as indicated by the two peaks of  $|e_{2y}|$  and the low probability of  $|e_{2z}|$  close to unity. This indicates that in the near wall region the plane of the curved fibers considered is most probably parallel to the  $x - y$  plane. In [28] we quantify the effect of fibre curvature on fiber orientation and we show that in the curvature range examined this effect is negligible. The near-wall preferential orientation of the fibers is used to investigate the effect on their rotation of the near wall mean shear—and in turn, of the mean vorticity, mainly oriented in the spanwise direction [62]. To this aim, we use the fiber rotation rates measured in the fiber-fixed frame and in the laboratory frame of reference. In the main panel of Fig. 5(c) we show, as a function of  $y^+$ , the mean squared rotation rates around the two fiber transversal axes,  $\langle \omega_2^2 \rangle \tau^2$  and  $\langle \omega_3^2 \rangle \tau^2$  and around the wall-normal and spanwise directions,  $\langle \omega_y^2 \rangle \tau^2$  and  $\langle \omega_z^2 \rangle \tau^2$ , respectively. Across the channel height, all rates follow nearly the same trend with a minimum in the central region and a peak at  $y^+ = 60$ . We observe that values for  $\langle \omega_y^2 \rangle \tau^2$  and  $\langle \omega_z^2 \rangle \tau^2$  are similar, and so are the values of  $\langle \omega_2^2 \rangle \tau^2$  and  $\langle \omega_3^2 \rangle \tau^2$ . In connection with the results on fiber orientation discussed before, this demonstrates no prevalent role of the mean shear or mean vorticity near the wall. As further evidence, in the inset of Fig. 5(c) we show the mean absolute rotation rates around the wall-normal ( $\omega_y$ ) and spanwise directions ( $\omega_z$ ) as a function of  $y^+$ : both exhibit similar magnitudes across the channel height, further demonstrating no major influence of the spanwise oriented mean shear. In a DNS study [63], it was observed that the rotational mechanical energy of inertia-less ( $St = 0$ ), high aspect ratio ( $\lambda = 10$ ) ellipsoids was dominated by angular velocity fluctuations rather than by the mean angular velocity. The former were associated with turbulent fluctuations, while the latter with the mean shear. Conversely, the rotational mechanical energy of inertial ellipsoids ( $St = 30$ ,  $\lambda = 0.1-10$ ) was found to be dominated by the mean angular velocity, so by the mean shear. This is also supported by experimental evidence [24], where the high tumbling rates of inertial rods ( $St = 6$ ,  $\lambda = 11.8$ ) were attributed to the mean shear.

With the aim of characterizing the dispersion and sedimentation rates of microplastics in oceanic turbulence, we analyzed the rotation rates of slightly curved, inertia-less fibers in turbulent channel flow. Their shape enables measurements of their full rotational dynamics both in the fiber and laboratory frame of reference. Our findings align with those in both homogeneous isotropic [43,46] and wall-bounded turbulence studies [24]. We find that the rotation rates of inertia-less fibers are dominated by turbulent fluctuations and not by the mean shear, that spinning rates are higher than tumbling rates [20,46,63], that the components of tumbling rates have similar values, and also the spanwise and wall-normal components of the rotation rates have similar values.

Our technique may be used in the future to study the interaction between fibers and a solid boundary. Future studies might employ simultaneous measurements of curved fibers and surrounding flow to examine how near-wall structures influence the alignment of the fiber plane with the  $x$ - $y$  plane.

*Acknowledgments*—The authors acknowledge Mr. F. Neuwirth and Mr. W. Jandl for their support in the design and construction of the experimental facility. V. G. acknowledges the financial support provided by (Fondo Sociale Europeo) S3 HEaD (Higher Education and Development) (Grant No. 1619942002). This research was funded in part by the Austrian Science Fund (FWF) [Grant DOI: 10.55776/P35505]. V. G. and A. S. also gratefully acknowledge funding from the (Progetti di Rilevante Interesse Nazionale) project “Advanced computations and experiments in turbulent multiphase flow” (Project No. 2017RSH3JY).

---

[1] G. A. Voth and A. Soldati, Anisotropic particles in turbulence, *Annu. Rev. Fluid Mech.* **49**, 249 (2017).  
 [2] L. Brandt and F. Coletti, Particle-laden turbulence: Progress and perspectives, *Annu. Rev. Fluid Mech.* **54**, 159 (2022).  
 [3] F. Lundell, L. D. Söderberg, and P. H. Alfredsson, Fluid mechanics of papermaking, *Annu. Rev. Fluid Mech.* **43**, 195 (2011).  
 [4] R. C. Moffet and K. A. Prather, In-situ measurements of the mixing state and optical properties of soot with implications for radiative forcing estimates, *Proc. Natl. Acad. Sci. U.S.A.* **106**, 11872 (2009).  
 [5] L. Sabban and R. van Hout, Measurements of pollen grain dispersal in still air and stationary, near homogeneous, isotropic turbulence, *J. Aerosol Sci.* **42**, 867 (2011).  
 [6] A. J. Heymsfield, Precipitation development in stratiform ice clouds: A microphysical and dynamical study, *J. Atmos. Sci.* **34**, 367 (1977).  
 [7] T. Pedley and J. O. Kessler, Hydrodynamic phenomena in suspensions of swimming microorganisms, *Annu. Rev. Fluid Mech.* **24**, 313 (1992).

[8] P. S. Ross, S. Chastain, E. Vassilenko, A. Etemadifar, S. Zimmermann, S.-A. Quesnel, J. Eert, E. Solomon, S. Patankar, A. M. Posacka *et al.*, Pervasive distribution of polyester fibres in the Arctic Ocean is driven by Atlantic inputs, *Nat. Commun.* **12**, 106 (2021).  
 [9] K. Ugwu, A. Herrera, and M. Gómez, Microplastics in marine biota: A review, *Mar. Pollut. Bull.* **169**, 112540 (2021).  
 [10] E. S. Gruber, V. Stadlbauer, V. Pichler, K. Resch-Fauster, A. Todorovic, T. C. Meisel, S. Trawoeger, O. Hollóczki, S. D. Turner, W. Wadsak *et al.*, To waste or not to waste: Questioning potential health risks of micro-and nanoplastics with a focus on their ingestion and potential carcinogenicity, *Expos. Health* **15**, 33 (2023).  
 [11] H. A. Leslie, M. J. Van Velzen, S. H. Brandsma, A. D. Vethaak, J. J. Garcia-Vallejo, and M. H. Lamoree, Discovery and quantification of plastic particle pollution in human blood, *Environ. Int.* **163**, 107199 (2022).  
 [12] I. Chubarenko, A. Bagaev, M. Zobkov, and E. Esiukova, On some physical and dynamical properties of microplastic particles in marine environment, *Mar. Pollut. Bull.* **108**, 105 (2016).  
 [13] L. K. Clark, M. H. DiBenedetto, N. T. Ouellette, and J. R. Koseff, Dispersion of finite-size, non-spherical particles by waves and currents, *J. Fluid Mech.* **954**, A3 (2023).  
 [14] D. Tatsii, S. Bucci, T. Bhowmick, J. Guettler, L. Bakels, G. Bagheri, and A. Stohl, Shape matters: Long-range transport of microplastic fibers in the atmosphere, *Environ. Sci. Technol.* **58**, 671 (2023).  
 [15] A. Huntington, P. L. Corcoran, L. Jantunen, C. Thaysen, S. Bernstein, G. A. Stern, and C. M. Rochman, A first assessment of microplastics and other anthropogenic particles in Hudson Bay and the surrounding eastern Canadian Arctic waters of Nunavut, *Facets* **5**, 432 (2020).  
 [16] M. Kooi and A. A. Koelmans, Simplifying microplastic via continuous probability distributions for size, shape, and density, *Environ. Sci. Technol. Lett.* **6**, 551 (2019).  
 [17] S. Parsa, E. Calzavarini, F. Toschi, and G. A. Voth, Rotation rate of rods in turbulent fluid flow, *Phys. Rev. Lett.* **109**, 134501 (2012).  
 [18] S. Brizzolara, M. E. Rosti, S. Olivieri, L. Brandt, M. Holzner, and A. Mazzino, Fiber Tracking Velocimetry for Two-Point Statistics of Turbulence, *Phys. Rev. X* **11**, 031060 (2021).  
 [19] M. Byron, J. Einarsson, K. Gustavsson, G. Voth, B. Mehlig, and E. Variano, Shape-dependence of particle rotation in isotropic turbulence, *Phys. Fluids* **27** (2015).  
 [20] L. Zhao, N. R. Challabotla, H. I. Andersson, and E. A. Variano, Rotation of nonspherical particles in turbulent channel flow, *Phys. Rev. Lett.* **115**, 244501 (2015).  
 [21] C. Marchioli and A. Soldati, Rotation statistics of fibers in wall shear turbulence, *Acta Mech.* **224**, 2311 (2013).  
 [22] C. Marchioli, L. Zhao, and H. Andersson, On the relative rotational motion between rigid fibers and fluid in turbulent channel flow, *Phys. Fluids* **28** (2016).  
 [23] K. Yang, L. Zhao, and H. I. Andersson, Mean shear versus orientation isotropy: Effects on inertialess spheroids, rotation mode in wall turbulence, *J. Fluid Mech.* **844**, 796 (2018).

- [24] L. J. Baker and F. Coletti, Experimental investigation of inertial fibres and disks in a turbulent boundary layer, *J. Fluid Mech.* **943**, A27 (2022).
- [25] S. Shaik and R. van Hout, Kinematics of rigid fibers in a turbulent channel flow, *Int. J. Multiphase Flow* **158**, 104262 (2023).
- [26] A. A. Hoseini, F. Lundell, and H. I. Andersson, Finite-length effects on dynamical behavior of rod-like particles in wall-bounded turbulent flow, *Int. J. Multiphase Flow* **76**, 13 (2015).
- [27] V. Giurgiu, G. C. A. Caridi, M. Alipour, M. De Paoli, and A. Soldati, The TU Wien Turbulent Water Channel: Flow control loop and three-dimensional reconstruction of anisotropic particle dynamics, *Rev. Sci. Instrum.* **94** (2023).
- [28] See Supplemental Material at <http://link.aps.org/supplemental/10.1103/PhysRevLett.133.054101> for additional details on (I) methodology, measurement volume, resolution, acquisition frequency, and sample size, which includes Refs. [23,26,28,29,31,32,40,42,44,59]; with details about (II) the PDF of dimensionless fiber curvature, which includes Refs. [40,42]; with details about (III) the rotation rates computation, which includes Refs. [23,24,33,34,44]; with details about (IV) the effect of sample size on mean squared tumbling and spinning rates at three wall-normal positions and on the PDF of the normalized squared tumbling rate, which includes Refs. [17,43]; with details on (V) the influence of curvature on mean squared spinning and tumbling rates and fiber orientation, which includes Ref. [23]; with details about (VI) the settling behavior of fibers due to the density mismatch with the working fluid, which includes Ref. [37].
- [29] M. Kind and H. Martin, *VDI-Wärmeatlas* (Springer Vieweg, Berlin, Heidelberg, 2013).
- [30] G. E. Elsinga, F. Scarano, B. Wieneke, and B. W. van Oudheusden, Tomographic particle image velocimetry, *Exp. Fluids* **41**, 933 (2006).
- [31] L. Jiang, Private Communication on the “Rotation of anisotropic particles in Rayleigh-Bénard turbulence,” published in *J. Fluid Mech.* **901**, A8 (2020). (2024).
- [32] L. Jiang, E. Calzavarini, and C. Sun, Rotation of anisotropic particles in Rayleigh-Bénard turbulence, *J. Fluid Mech.* **901**, A8 (2020).
- [33] W. S. Cleveland, Robust locally weighted regression and smoothing scatterplots, *J. Am. Stat. Assoc.* **74**, 829 (1979).
- [34] K. M. Lynch and F. C. Park, *Modern Robotics* (Cambridge University Press, Cambridge, England, 2017), p. 77.
- [35] R. D. Moser, J. Kim, and N. N. Mansour, Direct numerical simulation of turbulent channel flow up to  $Re_\tau = 590$ , *Phys. Fluids* **11**, 943 (1999).
- [36] J. C. Del Alamo, J. Jiménez, P. Zandonade, and R. D. Moser, Scaling of the energy spectra of turbulent channels, *J. Fluid Mech.* **500**, 135 (2004).
- [37] T. Bhowmick, J. Seesing, K. Gustavsson, J. Guettler, Y. Wang, A. Pumir, B. Mehlig, and G. Bagheri, Inertia induces strong orientation fluctuations of nonspherical atmospheric particles, *Phys. Rev. Lett.* **132**, 034101 (2024).
- [38] The Flocking Shop, DCA Flock, <https://www.theflockingshop.co.uk> (2022).
- [39] O. Bernstein and M. Shapiro, Direct determination of the orientation distribution function of cylindrical particles immersed in laminar and turbulent shear flows, *J. Aerosol Sci.* **25**, 113 (1994).
- [40] M. Alipour, M. De Paoli, and A. Soldati, Influence of Reynolds number on the dynamics of rigid, slender and non-axisymmetric fibres in channel flow turbulence, *J. Fluid Mech.* **934**, A18 (2022).
- [41] S. Bounoua, G. Bouchet, and G. Verhille, Tumbling of inertial fibers in turbulence, *Phys. Rev. Lett.* **121**, 124502 (2018).
- [42] M. Alipour, M. De Paoli, S. Ghaemi, and A. Soldati, Long non-axisymmetric fibres in turbulent channel flow, *J. Fluid Mech.* **916**, A3 (2021).
- [43] S. Parsa and G. A. Voth, Inertial range scaling in rotations of long rods in turbulence, *Phys. Rev. Lett.* **112**, 024501 (2014).
- [44] S. Shaik, S. Kuperman, V. Rinsky, and R. van Hout, Measurements of length effects on the dynamics of rigid fibers in a turbulent channel flow, *Phys. Rev. Fluids* **5**, 114309 (2020).
- [45] P. Mortensen, H. Andersson, J. Gillissen, and B. Boersma, Dynamics of prolate ellipsoidal particles in a turbulent channel flow, *Phys. Fluids* **20**, 093302 (2008).
- [46] T. B. Oehmke, A. D. Bordoloi, E. Variano, and G. Verhille, Spinning and tumbling of long fibers in isotropic turbulence, *Phys. Rev. Fluids* **6**, 044610 (2021).
- [47] G. G. Marcus, S. Parsa, S. Kramel, R. Ni, and G. A. Voth, Measurements of the solid-body rotation of anisotropic particles in 3D turbulence, *New J Phys.* **16**, 102001 (2014).
- [48] N. Pujara, J.-A. Arguedas-Leiva, C. C. Lalescu, B. Bramas, and M. Wilczek, Shape-and scale-dependent coupling between spheroids and velocity gradients in turbulence, *J. Fluid Mech.* **922**, R6 (2021).
- [49] S. Douady, Y. Couder, and M. E. Brachet, Direct observation of the intermittency of intense vorticity filaments in turbulence, *Phys. Rev. Lett.* **67**, 983 (1991).
- [50] J. Jimenez and A. A. Wray, On the characteristics of vortex filaments in isotropic turbulence, *J. Fluid Mech.* **373**, 255 (1998).
- [51] S. K. Robinson, Coherent motions in the turbulent boundary layer, *Annu. Rev. Fluid Mech.* **23**, 601 (1991).
- [52] R. J. Adrian, Hairpin vortex organization in wall turbulence, *Phys. Fluids* **19**, 041301 (2007).
- [53] Y. Yang and D. Pullin, Geometric study of Lagrangian and Eulerian structures in turbulent channel flow, *J. Fluid Mech.* **674**, 67 (2011).
- [54] M. A. Green, C. W. Rowley, and G. Haller, Detection of Lagrangian coherent structures in three-dimensional turbulence, *J. Fluid Mech.* **572**, 111 (2007).
- [55] J. Jiménez, Coherent structures in wall-bounded turbulence, *J. Fluid Mech.* **842**, P1 (2018).
- [56] A. Sharma and B. J. McKeon, On coherent structure in wall turbulence, *J. Fluid Mech.* **728**, 196 (2013).
- [57] N. R. Challabotla, L. Zhao, and H. I. Andersson, Shape effects on dynamics of inertia-free spheroids in wall turbulence, *Phys. Fluids* **27** (2015).
- [58] L. Zhao and H. I. Andersson, Why spheroids orient preferentially in near-wall turbulence, *J. Fluid Mech.* **807**, 221 (2016).
- [59] M. Do-Quang, G. Amberg, G. Brethouwer, and A. V. Johansson, Simulation of finite-size fibers in turbulent channel flows, *Phys. Rev. E* **89**, 013006 (2014).

- [60] Z. Cui, W.-X. Huang, C.-X. Xu, H. I. Andersson, and L. Zhao, Alignment of slender fibers and thin disks induced by coherent structures of wall turbulence, *Int. J. Multiphase Flow* **145**, 103837 (2021).
- [61] R. Ni, N.T. Ouellette, and G. A. Voth, Alignment of vorticity and rods with Lagrangian fluid stretching in turbulence, *J. Fluid Mech.* **743**, R3 (2014).
- [62] K. Iwamoto, Y. Suzuki, and N. Kasagi, Reynolds number effect on wall turbulence: Toward effective feedback control, *Int. J. Heat Fluid Flow* **23**, 678 (2002).
- [63] L. Zhao, N.R. Challabotla, H.I. Andersson, and E. A. Variano, Mapping spheroid rotation modes in turbulent channel flow: Effects of shear, turbulence and particle inertia, *J. Fluid Mech.* **876**, 19 (2019).